International Journal of Plasticity 67 (2015) 53–68

Contents lists available at ScienceDirect

International Journal of Plasticity

journal homepage: www.elsevier.com/locate/ijplas

Anisotropy and tension–compression asymmetry modeling of the room temperature plastic response of Ti–6Al–4V

V. Tuninetti [a,*], G. Gilles [a], O. Milis [a], T. Pardoen [b], A.M. Habraken [a,c]

[a] ARGENCO Department, MS²F Division, University of Liège, Chemin des Chevreuils 1, 4000 Liège, Belgium
[b] Institute of Mechanics, Materials and Civil Engineering, Université catholique de Louvain, Place Sainte Barbe 2, B-1348 Louvain-la-Neuve, Belgium
[c] Research Director of the Fonds de la Recherche Scientifique – FNRS, Belgium

ARTICLE INFO

Article history:
Received 3 March 2014
Received in final revised form 22 September 2014
Available online 18 October 2014

Keywords:
A. Yield condition
B. Anisotropic material
B. Constitutive behaviour
C. Mechanical testing
Inverse modeling

ABSTRACT

The mechanical behavior of the alloy Ti–6Al–4V is characterized using uniaxial tension, uniaxial compression, simple shear and plane strain tests in three orthogonal material directions. The experimental results reveal tension/compression asymmetry, anisotropic yielding and anisotropic strain-hardening. These features are incorporated into an elasto-plastic constitutive law based on the macroscopic orthotropic yield criterion "CPB06" adapted to hexagonal metals. A new identification method for the yield criterion parameters is proposed by inverse modeling of the axial strain field of compression specimens in the three orthogonal directions of the material. The sensitivity of different sets of material parameters to the identification method is also analyzed and the capacity of the model to accurately predict the forces and displacement field is discussed. A validation of the best set of identified CPB06 material parameters is performed by comparing the load–displacement curves in different loading directions for tensile tests on notched round bars with different levels of stress triaxiality and for compression tests on elliptical cross-section specimens, both tests involving multiaxial strain fields and large deformations.

1. Introduction

In engineering applications, titanium (Ti) and its alloys have replaced other metallic materials owing to superior strength to density ratio, giving reliable, economic and more sustainable systems and components. The most commonly used and relatively economical Ti alloy is the Ti–6Al–4V composition, called hereafter TA6V. This two phase $\alpha + \beta$-type alloy is found in many applications principally in the aerospace industry, such as for fasteners, aircraft structural and engine components, because of its high strength over density ratio in the low to moderate range of operating temperatures. Offshore petroleum industry have also taken advantages of using TA6V, for instance in applications as drilling risers owing its high flexibility (low ratio of modulus over strength), excellent corrosion and fatigue resistance (Deyuan et al., 2001; Gurrappa, 2003; Lütjering and Williams, 2007). These high mechanical performances combined with a good biocompatibility motivate extensive use of the TA6V in the medical industry such as orthopedic and dental implants (Elias et al., 2008; Long and Rack, 2006; Rack and Qazi, 2006). The high strength to weight ratio and its good ballistic capability have attracted the interest of the defense industry for its use in armor for military vehicles (Burkins et al., 2000, 2001; Montgomery and Wells, 2001; Sukumar et al., 2013).

* Corresponding author. Tel.: +32 43669219; fax: +32 43669192.
E-mail address: V.Tuninetti@ulg.ac.be (V. Tuninetti).

http://dx.doi.org/10.1016/j.ijplas.2014.10.003
0749-6419/

The wide range of applications of the TA6V has set the motivation to develop and enhance the state of modeling of its mechanical behavior involving the plastic response. The primary phase noted α of the alloy TA6V is a hexagonal closed packed (hcp) structure. As for other hcp alloys, the flow stress is strongly dependent on both temperature and strain rate (Khan et al., 2004, 2007; Lee and Lin, 1998; Majorell et al., 2002; Peirs et al., 2010; Tuninetti et al., 2012b; Tuninetti and Habraken, 2014; Porntadawit et al., 2014). In addition, TA6V exhibits a strength asymmetry between tension and compression also called strength differential (SD) effect (Gilles et al., 2011; Hammami et al., 2011; Khan et al., 2012; Odenberger et al., 2012; Tuninetti et al., 2012b). Gilles et al. (2011) and Nixon et al. (2010) explain that this effect is the result of the combination of a sharp initial basal texture and of the polarity of the deformation twinning mechanism, even for monotonic loadings. Because of the twinning and texture evolution, the shape of the yield surface of hcp metals significantly changes with accumulated plastic deformation and, therefore, traditional hardening laws cannot accurately capture these phenomena (Plunkett et al., 2006). Most of the previous studies have focused on capturing these features (SD, anisotropy) and the validation has been essentially based on the assessment of true stress-true strain curve predictions of monotonic tests.

The main objectives of the current study are to characterize, at Room Temperature (RT), the quasi-static mechanical behavior of TA6V alloy for different multi-axial stress states, to develop a methodology to identify the macroscopic orthotropic yield criterion CPB06 developed by Cazacu et al. (2006) and, finally, to verify the capabilities of Finite Element (FE) simulations, based on this constitutive model to predict the evolution of the load and shape changes due to plastic deformation in more complicated specimen geometries such as notched round bars and elliptical cross-sections.

Numerous models have been applied to simulate the quasi-static behavior of TA6V. Several studies rely on the Johnson–Cook or Norton-Hoff models to take into account the strain rate sensitivity of TA6V alloy even when the strain rate range is well below the dynamic regime (Kotkunde et al., 2014; Vanderhasten et al., 2008). These models neglect the strength differential effect and the plastic anisotropy. Other studies were focused on damage prediction, but assuming an isotropic behavior. For instance Peirs (2012), investigated the fracture behavior of the TA6V using either a Johnson–Cook damage initiation criterion combined with a progressive isotropic damage law or the Gurson model. In this study, the true fracture strain was around 40%. Damage in TA6V is known to proceed by the nucleation, growth and coalescence of small internal voids like in most other industrial metallic alloys, e.g. (Peirs, 2012; Lecarme, 2013). Now, a key result recently obtained using 3D in-situ tomography (Lecarme, 2013) is that the porosity in TA6V remains quite small almost until fracture (e.g., it is equal to 0.57% at true axial strain equal to $\sim$0.7) and that it nucleates late in the deformation process (at a true axial strain equal to $\sim$0.4 under uniaxial tension). In other words, the softening induced by damage is very small up to relatively large strain. The focus of the present paper is to check the ability of a phenomenological macroscopic anisotropic elasto-plastic law to predict TA6V plastic flow until equivalent strain typically lower than 0.3–0.6 for damage induced softening can be neglected.

Various constitutive laws have been developed such as the Khan–Huang–Liang (KHL) model (Khan and Liang, 1999) and its extensions (Khan and Yu, 2012; Khan et al., 2012), the asymmetric yield function with dependence on the stress invariants proposed by Yoon et al. (2014), the asymmetric yield function based on Hill 1948 (Verma et al., 2011) and the CPB06 yield criterion developed by Cazacu et al. (2006) which capture both the anisotropy due to texture evolution and the Strength Differential effect (SD). Other models for hcp metals include Cazacu and Barlat (2004) and Lou et al. (2013). The model by Cazacu and Barlat (2004) is simple as the principal stresses are not needed which simplifies the implementation on a FE code. The advantage of the model by Lou et al. (2013) lies in that both the anisotropy in yield stresses and *R*-values are considered under associated flow rule. The CPB06 criterion was selected in this work for its flexibility. A similar criterion was successfully employed by Plunkett et al. (2006, 2008), Cazacu et al. (2010), Nixon et al. (2010), Gilles et al. (2011), Ghaffari Tari et al. (2014) and Yoon et al. (2013).

The CPB06 phenomenological yield function described in Section 4 will be identified at RT and at a strain rate equal to $10^{-3}\,s^{-1}$ from a set of monotonic tests described in Section 2 involving uniaxial tensile, uniaxial compression, simple shear and plane strain tensile states. The "one step" identification method proposed earlier by Gilles et al. (2011) is replaced here by a more accurate 'two steps' method integrating inverse FE modeling described in Section 4.2. The anisotropic hardening behavior is described by linear interpolation of continuous CPB06 yield surfaces identified at several plastic work levels, which makes it possible the description of different hardening rates in tension, compression and shear. Inverse modeling including uniaxial stress–strain responses in tension, plane strain, shear as well as FE analyses of compression tests are used to adjust the material parameters. This identification method is first validated in Section 4.2 by predicting the experimental axial strain distribution measured by 3D digital image correlation (DIC) in the median cross-section of compression specimens with initially elliptic cross-section for three orthogonal material directions. A second validation is also presented in Section 5 by predicting the load evolution and shape of tensile notched round bars and of compression specimens.

Finally, the sensitivity of the different sets of identified material parameters to the identification method as well as the capacity of the model to accurately predict forces and displacement fields are discussed.

This research focuses not only on capturing the SD and anisotropy of TA6V alloy observed in monotonic stress–strain curves, but also on verifying that FE simulations can accurately reproduce the load and shape changes of full scale specimens subjected to multiaxial loading and large plastic strains.

2. Material and experimental procedures

Compression, tension, shear and plane strain specimens are machined from an initial TA6V alloy ingot with the dimensions shown in Fig. 1. Both tensile and compression tests are performed in the three orthogonal directions of the material:

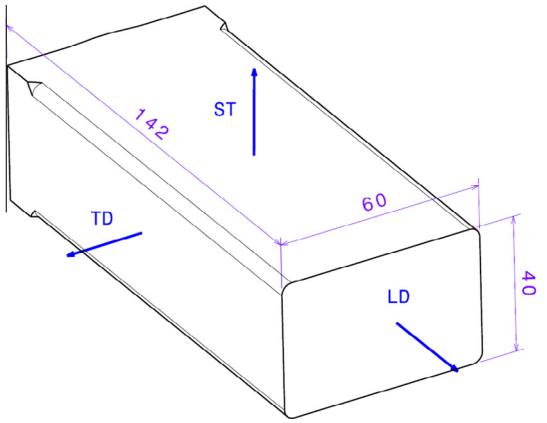

Fig. 1. Material directions of the TA6V ingot (dimensions in mm).

Longitudinal (LD), Transverse (TD) and Short Transverse (ST). Shear, Bauschinger and plane strain tensile tests are performed in the ST-LD plane. The tests are performed at room temperature and the targeted strain rate is constant, equal to 10^{-3} s^{-1}.

2.1. Material

The chemical composition of the TA6V alloy is given in Table 1. Optical microscopy shows slightly elliptic grains and with a mean grain size equal to 12 μm in the ST-LD plane and 9 μm in ST-TD plane. The α-phase represents 94% of the volume. The initial texture of the material shown in Fig. 2 was determined by X-ray diffraction (XRD) at Paris-13 University. The initial texture is quite weak.

2.2. Compression tests

Specimens are machined by wire electron discharge machining (EDM) with the dimensions shown in Fig. 3(a). The geometry used in this work was selected because the axial strain distribution and elliptical shape of the specimen is more sensitive to the plastic anisotropy of the material. The experiments are performed in three orthogonal material directions: LD, TD and ST. The servo hydraulic axial testing machine is controlled with a feedback loop system in order to impose constant strain rates equal to 10^{-3} s^{-1}. Three 3D optical measurement systems (6 CCD cameras) are used and the strain/displacement fields are measured for characterization and validation purposes (Fig. 3(b)). Due to friction, a slight barreling is observed and the stress state is not purely uniaxial. The stress–strain curves are obtained using the method proposed by Tuninetti et al. (2012a). The cross-section of the specimen is determined by fitting an ellipse on the experimental data. The average true axial stress is computed by dividing the load measured by the load cell with the current cross-section area. The true average axial strain is obtained by averaging the axial strain measured on the surface of the horizontal symmetric plane of the sample.

2.3. Uniaxial tensile tests

Axisymmetric specimens of 6 mm diameter for the LD direction are tested at constant strain rates equal to 10^{-3}, 10^{-2}, and 10^{-1} s^{-1} using a universal testing machine and three 3D-DIC systems are used for the strain/displacement measurements. By using the cross-section evolution of the tensile samples measured by DIC, a parameter similar to the "Lankford" coefficient used for sheets is computed. It is defined as the ratio of the strain rates in the TD direction and in the ST direction, i.e. $R_{LD} = \dot{\varepsilon}_{TD}/\dot{\varepsilon}_{ST}$ with $\dot{\varepsilon}_{TD} = \ln(b/r)/t$, $\dot{\varepsilon}_{ST} = \ln(a/r)/t$, and where r is the initial radius of the specimen and a, b are the major and minor axis lengths of the current elliptical cross-section of the specimen, while t is the time. Accurate cross-sectional area values are measured during the entire duration of the test. The average value of the axial stress can thus be computed even after the onset of necking. However, as such information was not available in TD and ST directions, it was decided to only use the pre-necking part of the curve. The load–displacement curve is identified until the earliest possible occurrence of necking by applying the Considère criterion.

The tensile tests in the TD and ST directions are performed on axisymmetric specimens of 4 mm in diameter using a universal testing machine equipped with a digital axial extensometer (Lecarme, 2013). The section is estimated by assuming volume conservation until the onset of necking which is identified by the Considère criterion. The machine is controlled in order to keep a constant cross-head speed. The stress strain curves obtained for average plastic strain rates equal to 7×10^{-4} s^{-1} for the TD and 9×10^{-5} s^{-1} for the ST direction are transformed into the corresponding response at a rate of

Table 1
Chemical composition of the TA6V alloy.

Al	V	Fe	N	O	C	Ti
6.1	4.0	0.3	0.05	0.20	0.08	Bal.

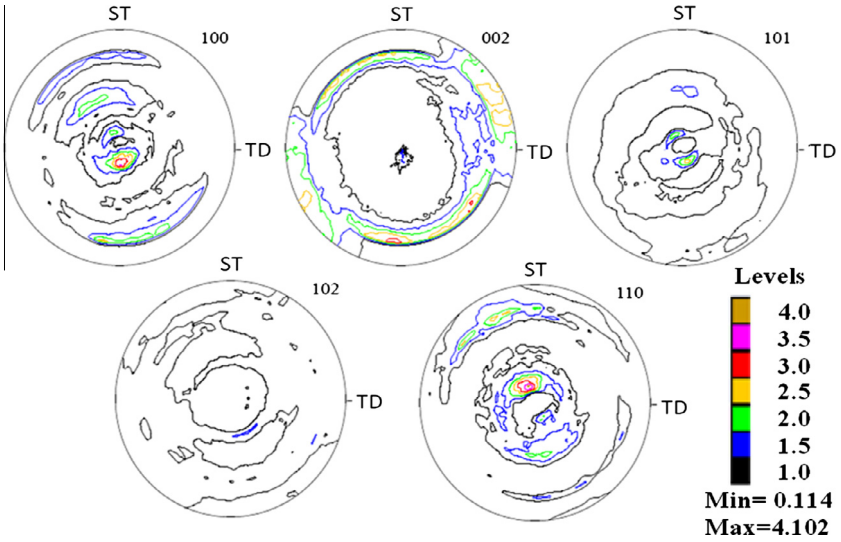

Fig. 2. Initial texture of the investigated TA6V alloy.

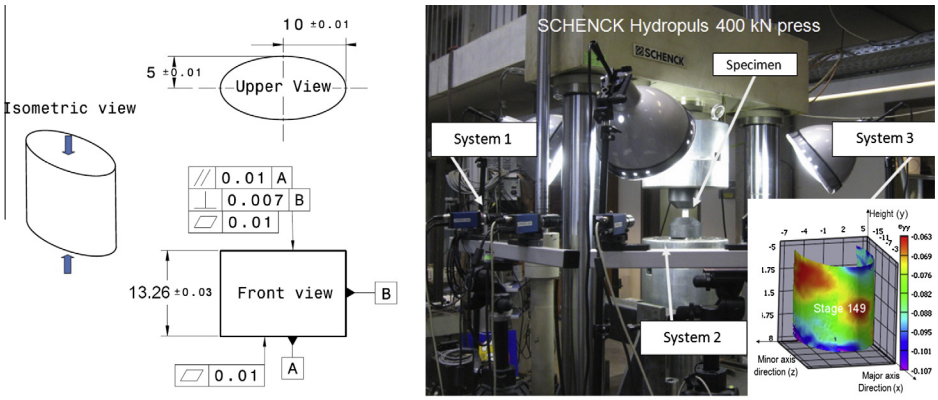

Fig. 3. Compression tests; (a) geometry and dimensions of the specimens in mm. (b) DIC system of 6 cameras provides axial strain fields.

10^{-3} s^{-1} (Tuninetti et al., 2012b). This minor correction was applied in order to identify the anisotropic yield locus at exactly the same strain rate (10^{-3} s^{-1}) in order to get rid of all possible rate dependent effects.

2.4. Simple shear, Bauschinger and plane strain tests

The tests are carried out on the specimens shown in Fig. 4 with the biaxial machine developed and validated by Flores et al. (2005) at the University of Liège. This machine uses vertical and horizontal actuators which control the displacement of the grips. These actuators are controlled in displacement at a constant speed. The plastic strain rate is equal to 10^{-3} s^{-1}. Two 3D-DIC systems are used for strain/displacement measurements. The true stress for plane strain tests is computed with the method proposed by Flores et al. (2010). This new accurate computational method uses the experimental data while including the edge effect evolution as a function of plastic strain. In the case of the shear tests, the edge effect is negligible

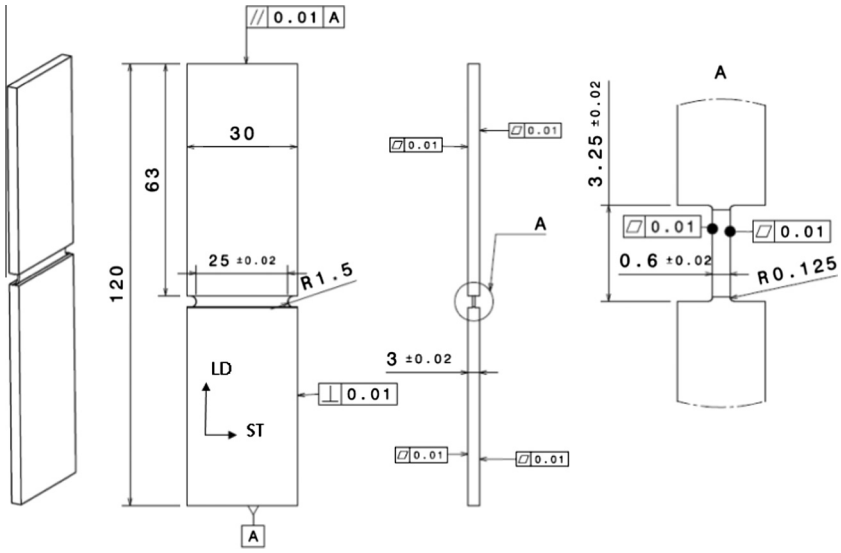

Fig. 4. The unique geometry and dimensions of specimen for plane strain, simple shear and Bauschinger test (dimensions in mm).

and the shear stress can be thus computed using: $\tau = F/A_0$, where F is the load and A_0 is the initial cross-section of the specimen.

Plane strain tension, plane strain compression, and pure shear constitute identical loading condition provided that the plastic deformation is independent of the hydrostatic pressure. This is because the Lode parameter is zero for all these three cases (Yoon et al., 2014; Lou et al., 2014). Hence, it is not necessary to conduct the pure shear test to calibrate the CPB06 yield function if plane strain tests data are available.

3. Experimental results

The average initial yield stress and the Young's modulus are provided in Table 2 with the standard deviations. The alloy exhibits anisotropic elastic properties at room temperature. Similar results were already reported by Olsen and Moreen (1973), Lanning et al. (2005) and Oldenber et al. (2012) and explained by the cylindrical symmetry of the HCP crystal structure (Tromans, 2011). For many materials, the Young's modulus in tension is found different from the Young's modulus in compression and it has to be derived from test data obtained in the stress mode of interest, as proposed by ASTM (2010). These elastic properties were mainly determined in this work using quasi-static uniaxial tension and compression tests with loading/unloading cycles near the onset of plasticity under constant strain rate of 10^{-3} s^{-1}. For the FE simulations described later, the apparent Young's modulus related to tension or compression state in the test direction (see Table 2) is used. Using a simple average Young's modulus value induces discrepancies in the measured and predicted load–displacement curves (Figs. 11, 15 and 16). The reason of the small difference between the Young's modulus in tension and in compression is not fully explained. This asymmetry leading to larger stiffness in compression compared to tension shows up only for sufficiently large elastic strains. The elastic strains reached in Ti alloys are indeed significant, on the order of + or −1% due to the large strength and relatively low stiffness which can then exhibit the expected asymmetry in the interatomic repulsion/attraction forces.

Fig. 5 gathers all the available curves at 10^{-3} s^{-1} strain rate and RT, based on an average experimental response for each loading direction and loading condition. The material response of the TA6V demonstrates a significant strength asymmetry between tension and compression. Anisotropic hardening is found and is observed to be stronger in compression compared

Table 2
Experimental Young's modulus and yield stress.

Test	Direction	Strain rate s^{-1}	Young's modulus E GPa/Std. Dev.	Yield strength σ_0 MPa (0.2% plastic strain)/Std. Dev.
Tension	LD	10^{-3}	111 ± 1	927 ± 3
	TD	10^{-3}	115 ± 4	933 ± 1
	ST	10^{-3}	117 ± 1	941 ± 4
Compression	LD	10^{-3}	122 ± 1	968 ± 3
	TD	10^{-3}	128 ± 3	1040 ± 6
	ST	10^{-3}	123 ± 3	1002 ± 5

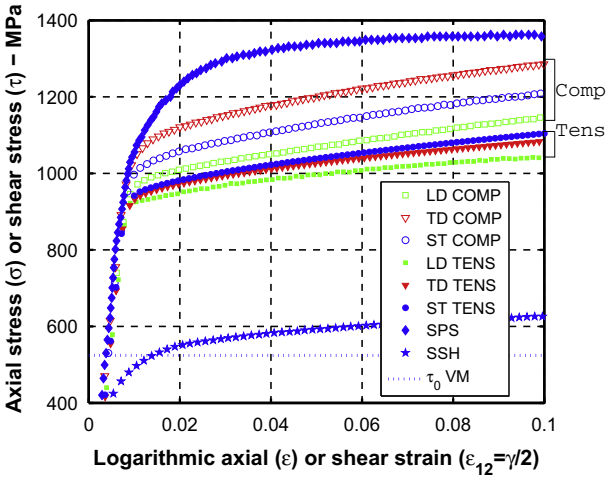

Fig. 5. True stress strain curves for monotonic tensile and compression in three orthogonal material directions (LD, TD and ST), plane strain (SPS in LD-ST plane), and simple shear (SSH in LD-ST plane) at 10^{-3} s^{-1} and at RT. The Voce hardening coefficients identified in tension along LD direction are $A_0 = 921.0$, $B_0 = 160.0$, $C_0 = 15.48$.

to tension. The usual definition of Lankford coefficient used in sheet plane to quantify the degree of anisotropy has to be adapted for this bulk material. The so called "*R* value" in tension and LD direction is measured during the tests by DIC identifying the evolution of the radii of the elliptic minimum cross-section. This value for the axial strain range [0,0.1] is almost constant and its average value will be used hereafter: $R_{LD} = \dot{\varepsilon}_{TD}/\dot{\varepsilon}_{ST} = 1.15$.

Often, isotropic hardening is related to an increase of the dislocation density during plasticity and can be modeled by a simple homothetic expansion of the yield locus. Here, the hardening behavior is more complex. As already observed by Lou et al. (2007) and Nixon et al. (2010), the hardening rate in the TA6V alloy is different in tension and in compression. It varies with the loading direction as well (Fig. 5). For this reason, in the next section, the fitting of the CPB06 yield locus with the monotonic experimental stress–strain data for several plastic work levels will take into consideration the updating of the shape of the yield criterion. The texture evolution and the effect of twinning are the primary reasons for these macroscopic observations.

4. Constitutive model and identification procedure

4.1. CPB06. Orthotropic yield criterion

The macroscopic orthotropic yield criterion CPB06 proposed by Cazacu et al. (2006) and Plunkett et al. (2006), was selected in this study, as it describes both the tension/compression asymmetry and the anisotropic behavior. This criterion is defined by

$$F_1 = (|\Sigma_1| - k\Sigma_1)^a + (|\Sigma_2| - k\Sigma_2)^a + (|\Sigma_3| - k\Sigma_3)^a \tag{1}$$

where k is a parameter which takes into account the strength differential effect (SD), a is the degree of homogeneity, Σ_1, Σ_2, Σ_3 are the principal values of the tensor Σ defined by $\Sigma = \mathbf{C} : \mathbf{S}$ where $\mathbf{C}$ is a fourth-order orthotropic tensor that accounts for the plastic anisotropy of the material and $\mathbf{S}$ is the deviator of the Cauchy stress tensor. The tensor $\mathbf{C}$ represented as Voigt notations is defined as follows

$$\mathbf{C} = \begin{bmatrix} C_{11} & C_{12} & C_{13} & 0 & 0 & 0 \\ C_{12} & C_{22} & C_{23} & 0 & 0 & 0 \\ C_{13} & C_{23} & C_{33} & 0 & 0 & 0 \\ 0 & 0 & 0 & C_{44} & 0 & 0 \\ 0 & 0 & 0 & 0 & C_{55} & 0 \\ 0 & 0 & 0 & 0 & 0 & C_{66} \end{bmatrix} \tag{2}$$

A methodology that allows describing directional hardening which accounts for the distortion of the yield locus of hexagonal materials has been proposed by Plunkett et al. (2006). It consists in determining the anisotropy coefficients corresponding to several fixed levels of accumulated plastic strain and then use a piece-wise linear interpolation to obtain the

yield surface corresponding to any level of accumulated plastic strain. Gilles et al. (2011) have used a similar methodology where the plastic work is used instead of the accumulated plastic strain. This second methodology is adopted here. The updated yield locus is described by

$$f(\boldsymbol{\sigma}, \bar{\varepsilon}_p) = \bar{\sigma}(\boldsymbol{\sigma}, \bar{\varepsilon}_p) - Y(\bar{\varepsilon}_p) \tag{3}$$

where $\bar{\sigma}$ is the equivalent stress according to the given yield criterion in Eq. (1) while $\bar{\varepsilon}_p$ is the equivalent plastic strain associated to $\bar{\sigma}$ using the work-equivalence principle (Hill, 1987), and $Y(\bar{\varepsilon}_p)$ is a reference hardening curve (the tensile stress–strain curve along LD direction is adopted in this study). The form of the latter is chosen as $Y(\bar{\varepsilon}_p) = A_0 + B_0\lfloor 1 - \exp\left(-C_0\bar{\varepsilon}_p\right)\rfloor$, where $A_0,\ B_0,\ C_0$ are material constants. For any $\bar{\varepsilon}_p$, the plastic work per unit volume is given by

$$W_p(\bar{\varepsilon}_p) = \int_0^{\bar{\varepsilon}_p} Y(p)dp = (A_0 + B_0)\bar{\varepsilon}_p - \frac{B_0}{C_0}\left(1 - \exp(-C_0\bar{\varepsilon}_p)\right). \tag{4}$$

The anisotropy coefficients and k parameters are considered to evolve as a function of the plastic work per unit volume W_p. They are determined for several levels of W_p: $W_p^{(1)} < \cdots < W_p^{(j)} < \cdots < W_p^{(m)}$, $j = i, \ldots, m$, where $W_p^{(1)}$ corresponds to initial yielding and $W_p^{(m)}$ corresponds to the highest level of plastic work attained in the experimental tests. Next, for each of the individual plastic work levels, $W_p^{(j)},\ \bar{\sigma}$ is calculated using Eq. (1). The determination of the yield surface corresponding to an intermediate level of plastic work ($W_p^{(j)} \leqslant W_p \leqslant W_p^{(j+1)}$) is made by a linear interpolation.

4.2. Identification procedure

The anisotropy coefficients C_{ij} and k parameters of the CPB06 yield criterion are fitted based on experimental yield stress ratios and the single R-ratio available using the Simulated Annealing (SA) algorithm (Metropolis et al., 1953; Hastings, 1970). This is a global optimization method that distinguishes between different local optima. In this study, the error function to be minimized is defined as follows

$$\begin{aligned} E = &\sum_{i=1}^{r}\eta_i\left[\frac{(\sigma_D^T/\sigma_{LD}^T)_i^{\text{num}}}{(\sigma_D^T/\sigma_{LD}^T)_i^{\text{exp}}} - 1\right]^2 + \sum_{j=1}^{s}\eta_j\left[\frac{(\sigma_D^C/\sigma_{LD}^T)_j^{\text{num}}}{(\sigma_D^C/\sigma_{LD}^T)_j^{\text{exp}}} - 1\right]^2 + \sum_{k=1}^{t}\eta_k\left[\frac{(\sigma_D^{SPS}/\sigma_{LD}^T)_k^{\text{num}}}{(\sigma_D^{SPS}/\sigma_{LD}^T)_k^{\text{exp}}} - 1\right]^2 + \cdots \\ &+ \sum_{l=1}^{u}\eta_l\left[\frac{(\sigma_D^{SSH}/\sigma_{LD}^T)_l^{\text{num}}}{(\sigma_D^{SSH}/\sigma_{LD}^T)_l^{\text{exp}}} - 1\right]^2 + \sum_{m=1}^{v}\eta_m\left[\frac{R_m^{\text{num}}}{R_m^{\text{exp}}} - 1\right]^2 \end{aligned} \tag{5}$$

where r, s, t, u and v are respectively the number of tensile, compressive, plane strain, shear yield stresses, and available R-ratio. The superscript indicates whether the value is experimental (exp) or numerical (num). Parameters $\eta_{i,j,k,l,m}$ are used to balance the weight of each term. In the current identification, uniaxial tensile and compression tests are available in the three directions RD, TD, ST, while plane strain and shear tests and R-ratio are available in the LD direction only. This first identification step provides an initial set of parameters that requires further adjustments.

Starting from this first set of material parameters, inverse modeling of the compression tests provides a second refined set of parameters. This second identification step compares the predicted response with the experimental axial strain distribution measured in the median cross-section of the specimens by 3D-DIC for LD, TD and ST directions. This second identification is essential as the axial strain distribution in the specimens with the selected elliptical cross-section is very sensitive to the material anisotropy, seen Tuninetti et al. (2012a). One-eighth of the compression specimens is modeled in the FE simulations within the updated Lagrangian FE code Lagamine developed by ArGEnCo Department of the University of Liège. The BWD3D finite element is selected. It is an 8-node 3D brick element with a mixed formulation adapted to large strains and large displacements. It involves a reduced integration scheme (with only one integration point) and an hourglass control technique. This element is based on the non-linear three-field (stress, strain and displacement) HU-WASHIZU variational principle (Belytschko and Bindeman, 1991; Duchêne et al., 2007; Simo and Hughes, 1986). In order to simulate friction between the dies and the surface of the specimen for compression tests, 3D CFI3D contact elements (Habraken and Cescotto, 1998) with 4 integration points and a Coulomb friction law are chosen. The Coulomb friction coefficient Φ is considered to be constant. A value $\Phi = 0.08$ is obtained by fitting the measured and predicted barreling. Finally, these two identification steps provide a material parameter set based on compression and tension tests in three directions (LD, TD, ST), shear, plane strain tests and R_{LD} value for 5 plastic work levels and imposing the constraint $C_{44} = C_{55} = C_{66}$ (Table 3).

The CPB06 constitutive model identified by the above procedure (the results of other identification strategies will be addressed in the next section) is compared to the experimental data, as shown in Figs. 6–8. Fig. 6 shows the yield surfaces along with the experimental data for five levels of plastic work. The values that are directly extracted from the tests are plotted with discrete symbols, e.g. compression and tension in the three orthogonal material directions. However, for the plane strain tensile test, the axial stress is computed using experimental data but the transverse is not known. Due to this, the experimental plane strain data is shown as dashed line corresponding to the axial stress value. Three 2D cuts of the yield surface are presented (LD-TD, LD-ST and TD-ST) as well as the π-plane projection. Note that irrespective of the level of plastic

Table 3
Coefficients of CPB06 yield function for TA6V and for 5 plastic works levels ($a = 2$) and values of $Y(\bar{\varepsilon}_p)$ identified in tension along LD direction.

W_p	k	C_{11}	C_{12}	C_{13}	C_{22}	C_{23}	C_{33}	$C_{44} = C_{55} = C_{66}$
1.857	−0.136	1	−2.373	−2.364	−1.838	1.196	−2.444	−3.607
9.377	−0.136	1	−2.495	−2.928	−2.283	1.284	−2.446	4.015
48.66	−0.165	1	−2.428	−2.920	1.652	−2.236	1.003	−3.996
100.2	−0.164	1	−2.573	−2.875	1.388	−2.385	0.882	−3.926
206.6	−0.180	1	−2.973	−2.927	0.534	−2.963	0.436	−3.883
LD Tension		A_0=921.0			B_0=160.0			C_0=15.48

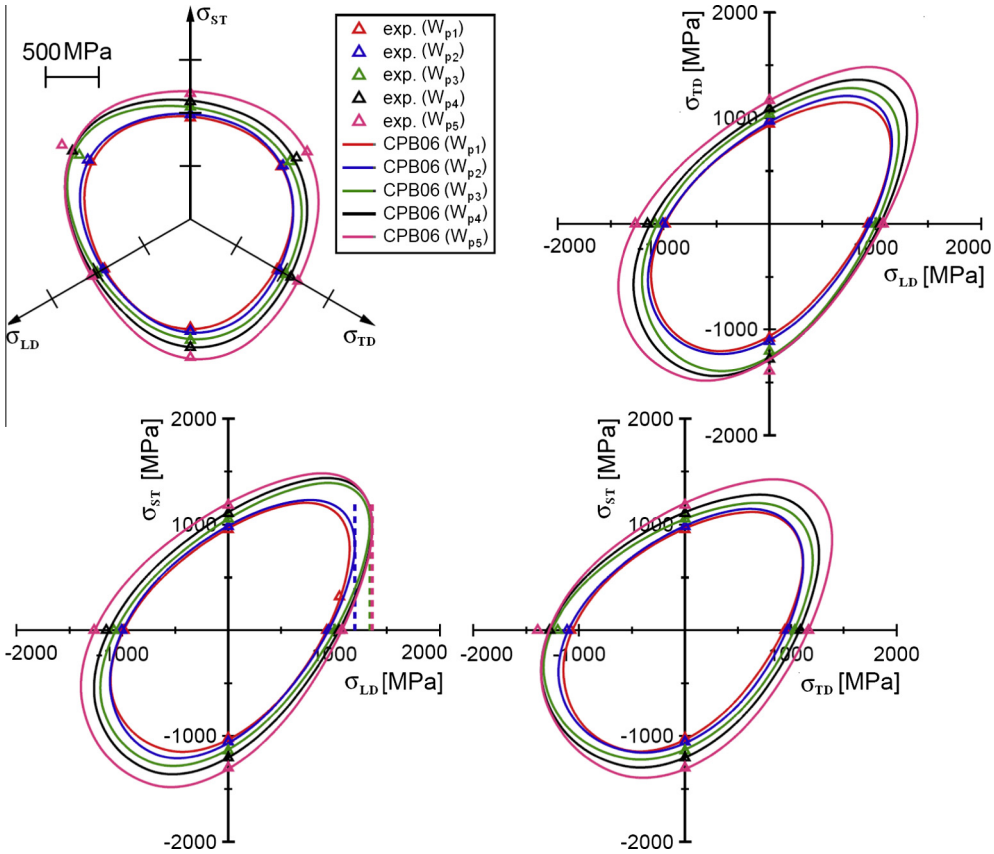

Fig. 6. Yield loci predicted by CPB06 and experimental points (exp.) for 5 accumulated plastic works: $W_{p1} = 1.86$, $W_{p2} = 9.38$, $W_{p3} = 48.7$, $W_{p4} = 100.2$ and $W_{p5} = 206.6$ J/cm^3.

work, the yield loci exhibit a distorted elliptical shape. The agreement between the model and experiments is quite satisfactory.

In order to analyze the plastic anisotropy predictions of the CPB06 model, the strain field predictions of compression tests in LD, TD and ST directions were also compared with the experimental results in Fig. 7 which provides the variation of the axial strain (along the surface of the middle cross-section of the compression samples) with the theta angle. The strain distribution is fairly well captured in the directions LD and TD but show a very large discrepancy in the ST direction. The maximum error is 17%. This error may be due to the fact that the R-value is not accurately modeled in the CPB06 yield function under the associated flow rule assumption.

Fig. 8 shows the experimental stress–strain curves along with the model predictions. Except for the compression in the TD direction, the predictions are consistent with the experiments. The different curves for both tension and compression in three directions (LD, TD and ST) clearly confirm that the von Mises isotropic approach is insufficient to describe the mechanical behavior of the TA6V alloy. The linear parts within the predicted curves in Fig. 8 reflect the fact that the hardening behavior is related to interpolation between different yield locus shapes identified for five plastic work levels.

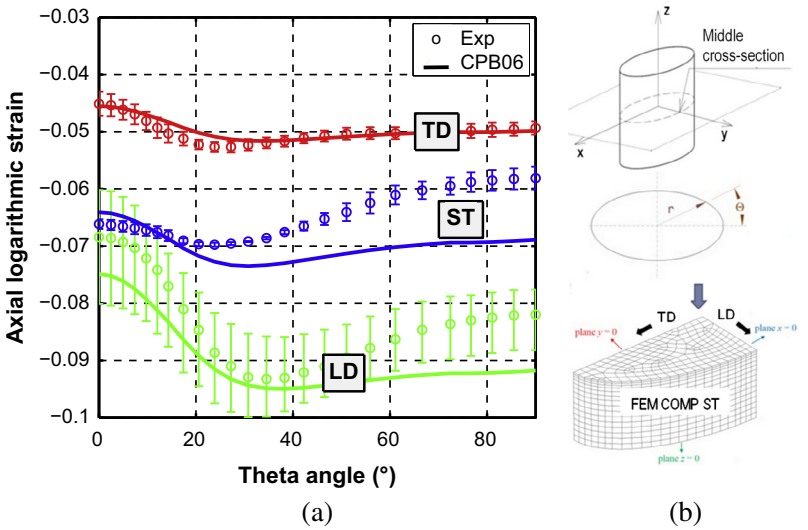

Fig. 7. Experimental (DIC) and CPB06 predictions of axial strain distribution along the surface of the middle cross-section of compression samples for LD at ε_{axial} = 0.08%, TD at ε_{axial} = 0.05% and ST at ε_{axial} = 0.065% (axial strain levels are reached for 200 kN of axial load).

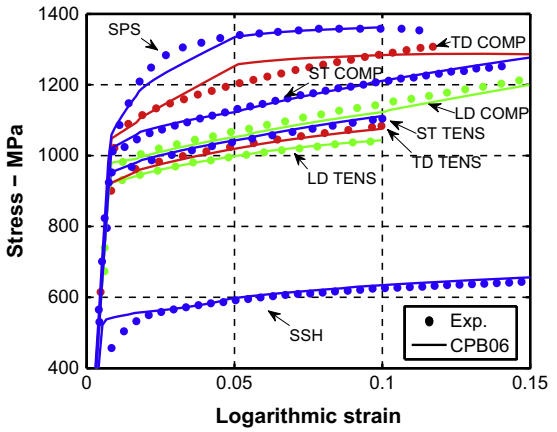

Fig. 8. Experimental (Exp.) and CPB06 predictions of stress–strain curves in tension (TENS) and in compression (COMP) for the LD, TD and ST directions, plane strain tensile LD-ST (SPS) and simple shear (SSH) LD-ST. The Voce hardening coefficients identified in tension along LD direction are A_0 = 921.0, B_0 = 160.0, C_0 = 15.48.

5. Applications and validation of the identified model

Tensile tests on notched specimens with two geometries R1.5 and R5 (Fig. 9) and a compression test on elliptical cross-section specimen (Fig. 3(a)) are used in order to validate the identified CPB06 model on stress states different than the one used for identification. The results of the simulation in Fig. 10 indicate different initial and "final" (for axial strain near fracture) stress triaxiality distributions along the radius of the minimum cross section for both notched specimens. Note that the triaxiality is defined as the ratio of the mean stress to the equivalent stress calculated according to the CPB06 criterion

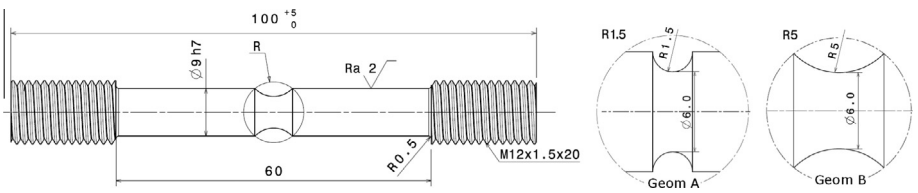

Fig. 9. Specimen geometries R1.5 and R5 for notched tensile tests in LD direction (dimensions in mm).

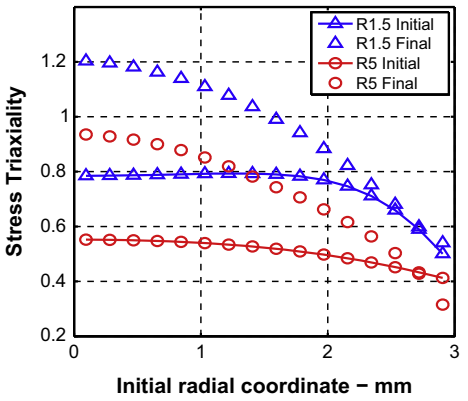

Fig. 10. Stress Triaxiality distribution along the radius of the minimum cross section for notched tensile tests geometries R1.5 and R5 at initial and final stage. The axial displacement at the final stage is equal to 0.8 mm for the specimens R1.5 and 1 mm for the specimens R5.

(Eq. (1)) and using the material parameters shown in Table 3. The numerical simulations are run within the updated Lagrangian FE code Lagamine already introduced in the previous section.

In Fig. 11(a) and (b), the variation of the load as a function of the displacement for a 40 mm gauge zone and the experimental dimensions of the cross-section of the specimens R1.5 just before fracture measured by 3D-DIC are compared with the predictions of the CPB06 model based on 4 different sets of material parameters identified with different choices of experimental test data:

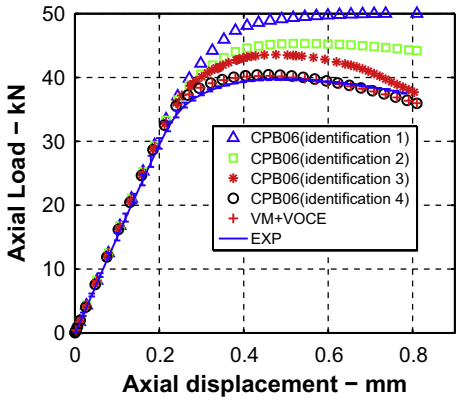

(a)

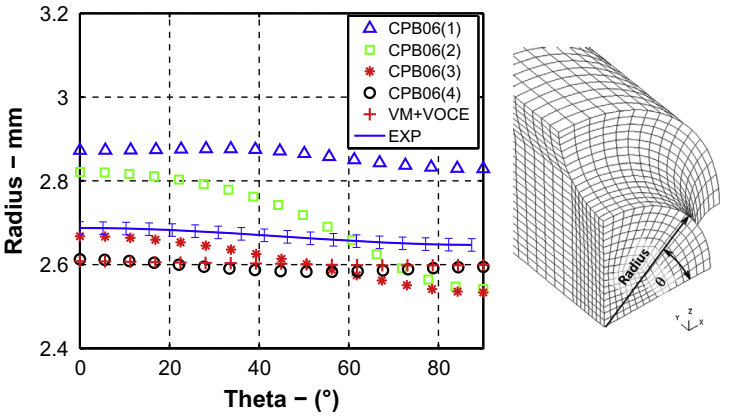

(b) (c)

Fig. 11. CPB06 predictions of the (a) load vs. displacement for specimen geometry R1.5 (40 mm gauge length) (b, c) cross-section of the specimen R1.5 at 0.8 mm of axial displacement.

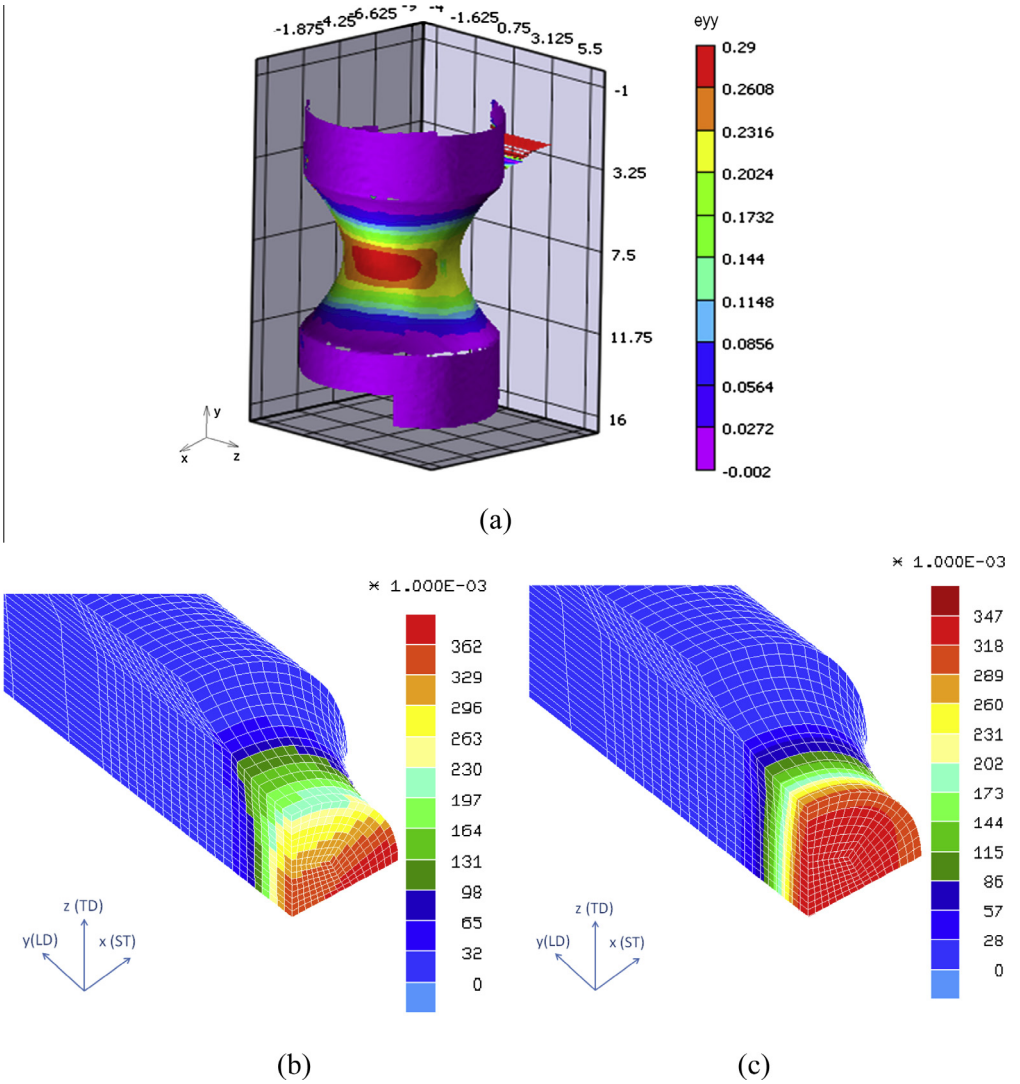

Fig. 12. Comparison of axial strain field ε_{yy} for geometry R5 at 1 mm of axial displacement in LD direction. (a) Measured by 3D-DIC (b) predicted by CPB06(3) and (c) by CPB06(4).

1. Initial CPB06 yield locus identified with compression and tension tests for LD, TD and ST with Voce type hardening law (isotropic hardening, the shape evolution of the yield criterion is neglected); under the name CPB06(1).
2. Initial CPB06 yield locus identified with compression and tension tests for LD, TD and ST, shear and plane strain tests with Voce type hardening law; under the name CPB06(2).
3. CPB06 identified with compression and tension tests for LD, TD and ST, shear, plane strain tests and $R_{LD} = 1.15$ value for 5 plastic work levels; under the name CPB06(3).
4. CPB06 identified with compression and tension tests for LD, TD and ST, shear, plane strain tests and $R_{LD} = 1.15$ value for 5 plastic work levels, with the two step identification method presented earlier and imposing $C_{44} = C_{55} = C_{66}$ (data set used for Figs. 6–8), under the name CPB06(4).

The results of Fig. 11 show that the identification procedures involving the largest number of monotonic tests (CPB06(3) and CPB06(4)) better reproduce both the load prediction and the shape of the deformed cross-section of the sample. However, the constraint of $C_{44} = C_{55} = C_{66}$ used for the identification CPB06(4) is needed in order to insure an accurate prediction of the load evolution. This constraint could be relaxed if shear tests for each material direction were available. Note that for this specific notched geometry loaded in the LD direction and reaching only moderate axial strain levels, the isotropic elasto-plastic von Mises law fitted on tensile tests in this direction predicts quite well both the load and average radius evolutions. However, as presented hereafter, the second specimen B, with a smoother notch radius (R5) and thus allowing larger plastic

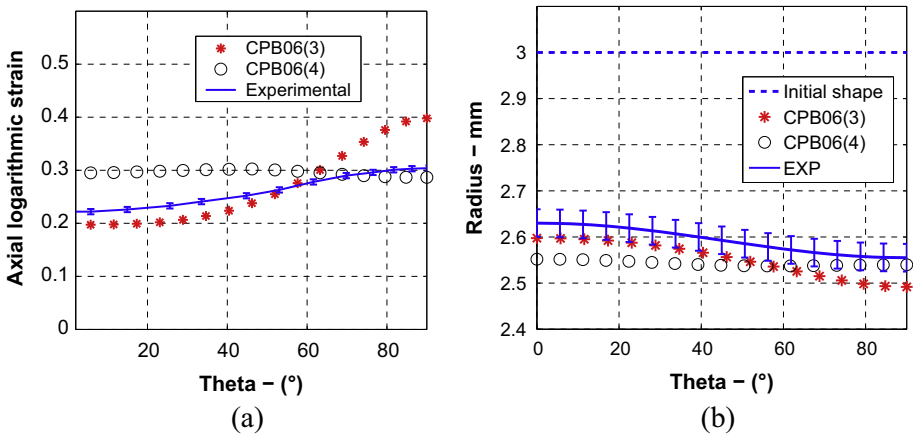

Fig. 13. Comparison of CPB06(3) and CPB06(4) predictions with DIC measurements for the specimen geometry R5 at 1 mm of axial displacement; (a) axial strain distribution in the minimum cross-section of specimen; (b) cross-section of specimen.

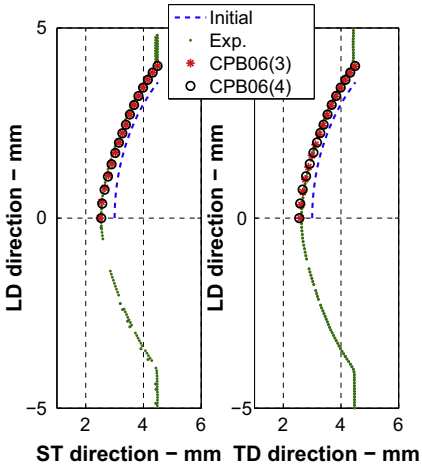

Fig. 14. Comparison of predicted CPB06(3) and CPB06(4) deformed shapes of the notch of the specimen R5 (at 1 mm of axial displacement) with DIC measurements.

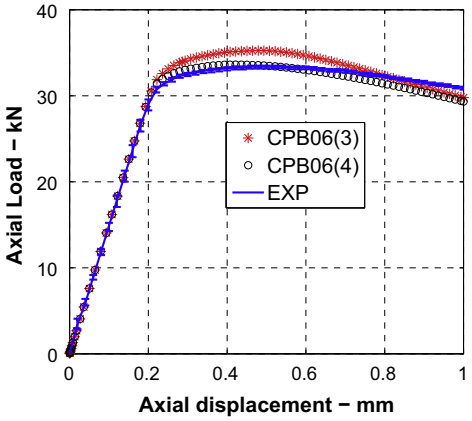

Fig. 15. Correlations of predicted load vs. displacement curve with experimental results of specimen R5.

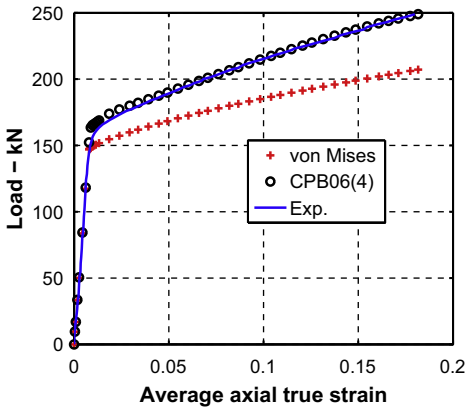

Fig. 16. Load vs. axial true strain predicted by CPB06(4) and measured in the experiment for compression tests in ST direction.

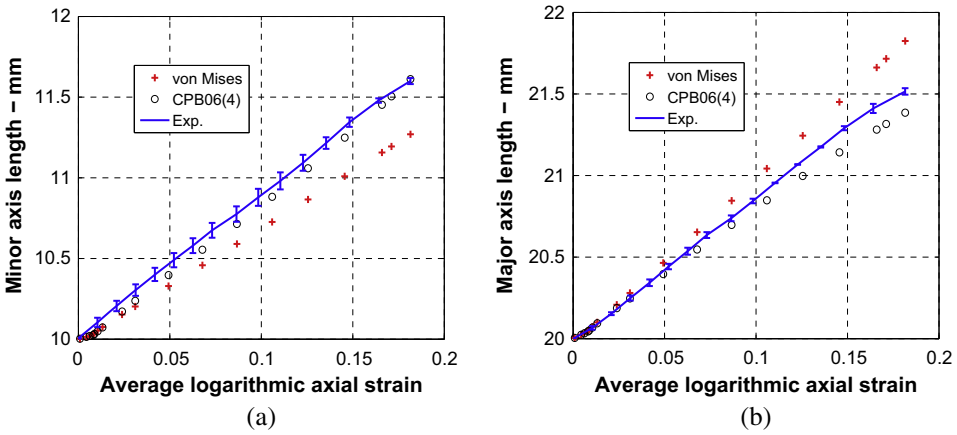

Fig. 17. Comparison between DIC measurements, CPB06(4) and von Mises law predictions of minor (a) and major (b) axis length of the elliptic cross-section of compression sample in ST direction.

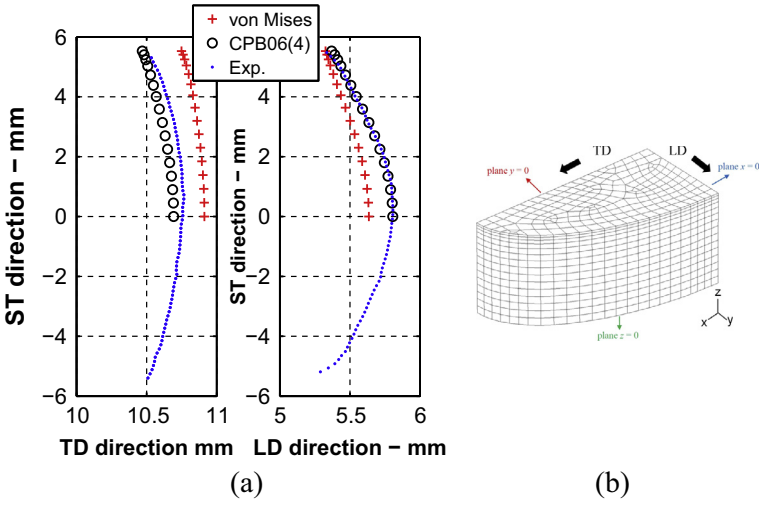

Fig. 18. Barreling predictions by CPB06(4) and von Mises law compared to experimental measurements obtained by DIC.

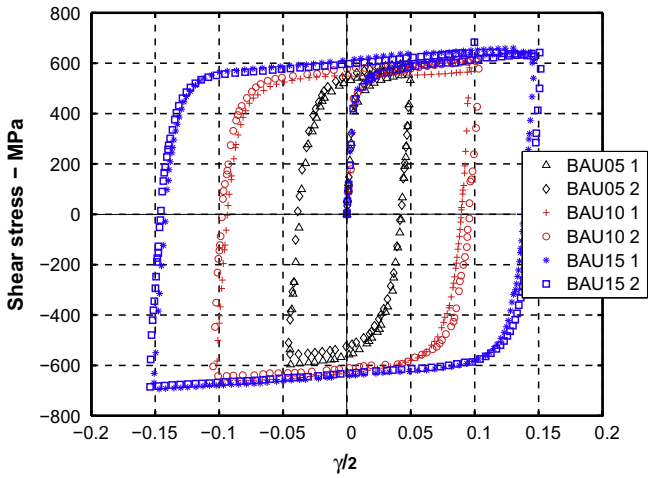

Fig. A1. Shear stress vs. shear strain curves for Bauschinger (BAU) tests at 05%, 10% and 15% shear prestrains. Two tests for each shear level are shown (1 and 2).

Table A1
Bauschinger ratios as a function of pre-strain measured in shear tests for TA6V.

Pre-strain (%)	*Br* (1st unloading)	*Br* (2nd unloading)
5	0.77	0.73
10	0.72	0.69
15	0.69	0.67

deformation before fracture confirms that, even for the LD direction, the von Mises law is not adapted due to plastic anisotropy (see Fig. 12(a)).

The second tensile tests on specimens with a medium notch radius (specimen R5: reaching a maximum stress triaxiality of 0.93 near fracture while the other notched geometry R1.5 reaches 1.2) have also been simulated. The section before fracture (Fig. 13(b)) involves a much larger distortion towards an elliptical shape compared to R1.5 (Fig. 11(b)) confirming that the von Mises (VM) isotropic approach is clearly insufficient. The results obtained from FEM by using the CPB06(3) and CPB06(4) are compared to the experimental measurements in Figs. 12–14. Inhomogeneous strain (Figs. 12(a) and 13(a)) fields and an elliptic shape of the cross-section (Fig. 13(b)) were observed just before fracture. The data measured by DIC are properly predicted by the CPB06 model identified with both sets of parameters and with an improved accuracy for set 3 (Figs. 12 and 13). The shape of notch just before fracture was also assessed in Fig. 14 and is in close agreement with the DIC measurements. Load vs. axial displacement comparisons in Fig. 15 reveal that imposing the constraint $C_{44} = C_{55} = C_{66}$ does not significantly affect the quality of the prediction, however CPB06(4) is still more accurate.

The DIC experimental measurements for the compression tests in the ST direction were compared to the FE results obtained with the parameter set CPB06(4) and with the von Mises law as well. Fig. 16 provides a comparison between the experimental results and the load predictions for the optimal value of friction coefficient $\Phi = 0.08$ with the CPB06(4) model and with the von Mises model using a hardening law based on a mean stress–strain curve corresponding to uniaxial tension in the LD direction. The elliptic shape of the middle cross-section of the compression specimen is modified during the test (Fig. 17). This effect was expected due to the friction between the dies and the sample and due to plastic anisotropy of the material as well. The effect of the friction is exhibited in Fig. 18 by comparing the predicted barreling with the DIC measurements.

6. Conclusions

The quasi-static mechanical response of a TA6V alloy was studied based on a wide set of mechanical tests performed at room temperature and at a low strain rate (10^{-3} s^{-1}) revealing both yield stress anisotropy and tension/compression asymmetry. Furthermore, the anisotropy in compression is more pronounced than in tension. Then, the experimental data were used in order to identify the material parameters of the CPB06 yield criterion. A new identification method for the yield criterion was proposed by using the inverse modeling of the axial strain field of compression specimens in the three orthogonal directions of the material. The validity of the model was studied for quasi-static strain rate and room temperature. This model captured most of the experimental features:

1. in monotonic tests: the distortion of the yield surface associated with the tension–compression asymmetry and the anisotropic hardening;
2. in specimens with multiaxial stress–strain states and several stress triaxialities (notched tensile tests and compression tests): load, shape changes and strain fields for different loading directions (tensile tests in LD, compression in ST directions).

The simulations demonstrated that the set of material parameters identified based on the largest number of tests and taking into account the evolution of the yield locus shape provides the best agreement with the experimental measurements used for validation. The interest of prescribing identical shear behavior in the 3 orthogonal planes when only one experiment is available, gives good predictions of load evolution (Figs. 11(a) and 15) but moderate discrepancies appear when looking at the strain distributions (Figs. 11(b), 12 and 13(a)). There are not enough anisotropic parameters in the CPB06 yield function to characterize the anisotropy both in the yield stresses and *R*-values. A non-associated flow rule could be applied to capture the anisotropy in *R*-values and therefore to reduce the discrepancies in the prediction of the strain distributions while still using the CPB06 function.

Future work must be performed in order to identify the evolution of the yield surface with strain rate, temperature, strain path changes and cyclic behavior and to incorporate kinematic hardening (Appendix A). The simplest version of the Cazacu model with one linear transformation (matrix **C** Eq. (2)) was used; however, increasing the number of transformations could provide even higher flexibility to the model.

Furthermore, the effect of damage should be investigated to predict fracture as well as to capture some moderate softening expected near the onset of fracture. Versions of the Gurson model extended to anisotropic yield locus like the one developed by Bettaïeb et al. (2011), Khan and Liu (2012) or Benzerga et al. (2004) can be used for this purpose. Nevertheless, the fact that the present model with no softening was able to reproduce the load and geometry evolution up to large strains confirms the assumption that damage in this material nucleates late with limited porosity levels until final stage of the coalescence process (Lecarme, 2013).

Acknowledgments

The authors thank the Walloon Region (Winnomat 2 project), the Belgian Scientific Research Fund FNRS which finances A.M.H. and the Interuniversity Attraction Poles Program, P7/21 Intemate initiated by the Belgian Science Policy office, for financial support. The authors would also like to thank B. Bacroix and T. Chauveau (U. Paris 13) for the texture measurements as well as L. Lecarme (UCL) for providing stress-strain curves in ST and TD directions used in this paper.

Appendix A. Quantification of kinematic hardening

Fig. A1 shows the variation of the shear stress ($\tau = F/A_0$) with the shear strain ($\gamma/2$). Three pre-strain 5, 10 and 15% of shear strain tests are presented. The reverse curves show early re-yielding and rapid work hardening. This significant kinematic hardening is quantitatively presented by using the Bauschinger ratio (Br) defined by

$$\mathrm{Br} = \frac{\sigma_f - \sigma_R}{2\sigma_F}, \quad (Br \leqslant 1) \tag{A.1}$$

where σ_F is the yield stress at the start of unloading and σ_R is the yield stress at the reverse loading (Table A1). Br is equal to 1 for pure isotropic hardening ($\sigma_f = -\sigma_R$). The smaller the Bauschinger ratio, the larger the Bauschinger effect. The presence of different stress levels within the α and β phases of the TA6V as well as the heterogeneity of the strain at the local level (twins and grain orientation implying different active slip systems with different critical resolved shear) explain the origin of the kinematic hardening.

References

ASTM, 2010. Standard Test Method for Young's Modulus, Tangent Modulus, and Chord Modulus. ASTM E111-04.
Belytschko, T., Bindeman, L.P., 1991. Assumed strain stabilization of the 4-node quadrilateral with 1-point quadrature for nonlinear problems. Comput. Methods Appl. Mech. Eng. 88, 311–340.
Benzerga, A.A., Besson, J., Pineau, A., 2004. Anisotropic ductile fracture: Part II: theory. Acta Mater. 52, 4639–4650.
Bettaieb, M.B., Lemoine, X., Duchêne, L., Habraken, A.M., 2011. On the numerical integration of an advanced Gurson model. Int. J. Numer. Methods Eng. 85, 1049–1072.
Burkins, M., Hansen, J., Paige, J., Turner, P., 2000. The Effect of Thermomechanical Processing on the Ballistic Limit Velocity of Extra Low Interstitial Titanium Alloy Ti–6Al–4V. U.S. Army Research Laboratory ARL-MR-486, 1–69.
Burkins, M., Wells, M., Fanning, J., Roopchand, B., 2001. The Mechanical and Ballistic Properties of an Electron Beam Single Melt of Ti–6Al–4V Plate. U.S. Army Research Laboratory, ARL-MR-515.
Cazacu, O., Barlat, F., 2004. A criterion for description of anisotropy and yield differential effects in pressure-insensitive metals. Int. J. Plasticity 20, 2027–2045.
Cazacu, O., Plunkett, B., Barlat, F., 2006. Orthotropic yield criterion for hexagonal close packed metals. Int. J. Plasticity 22, 1171–1194.
Cazacu, O., Ionescu, I.R., Yoon, J.W., 2010. Orthotropic strain rate potential for the description of anisotropy in tension and compression of metals. Int. J. Plasticity 26, 887–904.
Deyuan, F., Fort III, W., Horvath, R., 2001. Experience with titanium heat exchangers in refinery services. Mater. Perform. 40, 56–60.

Duchêne, L., El Houdaigui, F., Habraken, A.M., 2007. Length changes and texture prediction during free end torsion test of copper bars with FEM and remeshing techniques. Int. J. Plasticity 23, 1417–1438.
Elias, C.N., Lima, J.H.C., Valiev, R., Meyers, M.A., 2008. Biomedical applications of titanium and its alloys. JOM 60, 46–49.
Flores, P., Rondia, E., Habraken, A.M., 2005. Development of an experimental equipment for the identification of constitutive laws. Int. J. Forming Process. (Special Issue), 117–137.
Flores, P., Tuninetti, V., Gilles, G., Gonry, P., Duchêne, L., Habraken, A.M., 2010. Accurate stress computation in plane strain tensile tests for sheet metal using experimental data. J. Mater. Process. Technol. 210, 1772–1779.
Ghaffari Tari, D., Worswick, M.J., Ali, U., Gharghouri, M.A., 2014. Mechanical response of AZ31B magnesium alloy: experimental characterization and material modeling considering proportional loading at room temperature. Int. J. Plasticity 55, 247–267.
Gilles, G., Hammami, W., Libertiaux, V., Cazacu, O., Yoon, J.H., Kuwabara, T., Habraken, A.M., Duchêne, L., 2011. Experimental characterization and elasto-plastic modeling of the quasi-static mechanical response of TA–6V at room temperature. Int. J. Solids Struct. 48, 1277–1289.
Gurrappa, I., 2003. Characterization of titanium alloy Ti–6Al–4V for chemical, marine and industrial applications. Mater. Charact. 51, 131–139.
Habraken, A.M., Cescotto, S., 1998. Contact between deformable solids: the fully coupled approach. Math. Comput. Modell. 28, 153–169.
Hammami, W., Tirry, W., Coghe, F., Duchêne, L., Delannay, L., Habraken, A.M., 2011. Ti6A14V anisotropy and texture evolution predictions using multisite and self consistent crystal plasticity models. In: The 12th World Conference on Titanium Ti-2011.
Hastings, W.K., 1970. Monte Carlo sampling methods using Markov chains and their applications. Biometrika 57, 97–109.
Hill, R., 1987. Constitutive dual potentials in classical plasticity. J. Mech. Phys. Solids 35, 23–33.
Khan, A.S., Liang, R., 1999. Behaviors of three BCC metal over a wide range of strain rates and temperatures: experiments and modeling. Int. J. Plasticity 15, 1089–1109.
Khan, A.S., Liu, H., 2012. Strain rate and temperature dependent fracture criteria for isotropic and anisotropic metals. Int. J. Plasticity 37, 1–15.
Khan, A.S., Yu, S., 2012. Deformation induced anisotropic responses of Ti–6Al–4V alloy. Part I: experiments. Int. J. Plasticity 38, 1–13.
Khan, A.S., Suh, Y.S., Kazmi, R., 2004. Quasi-static and dynamic loading responses and constitutive modeling of titanium alloys. Int. J. Plasticity 20, 2233–2248.
Khan, A.S., Kazmi, R., Farroch, B., 2007. Multiaxial and non-proportional loading responses, anisotropy and modeling of Ti–6Al–4V titanium alloy over wide ranges of strain rates and temperatures. Int. J. Plasticity 23, 931–950.
Khan, A.S., Yu, S., Liu, H., 2012. Deformation induced anisotropic responses of Ti–6Al–4V alloy Part II: a strain rate and temperature dependent anisotropic yield criterion. Int. J. Plasticity 38, 14–26.
Kotkunde, N., Deole, A.D., Gupta, A.K., Singh, S.K., 2014. Comparative study of constitutive modeling for Ti–6Al–4V alloy at low strain rates and elevated temperatures. Mater. Des. 55, 999–1005.
Lanning, D., Nicholas, T., Haritos, G., 2005. On the use of critical distance theories for the prediction of the high cycle fatigue limit stress in notched Ti–6Al–4V. Int. J. Fatigue 27, 45–57.
Lecarme, L., 2013. Viscoplasticity, Damage and Fracture of Ti–6Al–4V. PhD Thesis. Université Catholique de Louvain, Belgium.
Lee, W.S., Lin, C.F., 1998. Plastic deformation and fracture behaviour of TA6V alloy loaded with high strain rate under various temperatures. Mater. Sci. Eng. A 241, 48–59.
Long, M., Rack, H.J., 2006. Titanium alloys in total joint replacement—a materials science perspective. Biomater 19, 1621–1639.
Lou, X.Y., Li, M., Boger, R.K., Agnew, S.R., Wagoner, R.H., 2007. Hardening evolution of AZ31B Mg sheet. Int. J. Plasticity 23, 44–86.
Lou, Y., Huh, H., Yoon, J.W., 2013. Consideration of strength differential effect in sheet metals with symmetric yield functions. Int. J. Mech. Sci. 66, 214–223.
Lou, Y., Yoon, J.W., Huh, H., 2014. Modeling of shear ductile fracture considering a changeable cut-off value for stress triaxiality. Int. J. Plasticity 54, 56–80.
Lütjering, G., Williams, J.C., 2007. Titanium: Engineering Materials and Processes, second ed. Springer-Verlag, Berlin.
Majorell, A., Srivatsa, S., Picu, R.C., 2002. Mechanical behavior of TA6V at high and moderate temperatures – Part I: experimental results. Mater. Sci. Eng. A 326, 297–305.
Metropolis, N., Rosenbluth, A.W., Rosenbluth, M.N., Teller, A.H., Teller, E., 1953. Equation of state calculations by fast computing machines. J. Chem. Phys 21, 1087–1092.
Montgomery, J.S., Wells, M.G.H., 2001. Titanium armor applications in combat vehicles. JOM 53, 29–32.
Nixon, M.E., Cazacu, O., Lebensohn, R.A., 2010. Anisotropic response of high-purity α-titanium: experimental characterization and constitutive modeling. Int. J. Plasticity 26, 516–532.
Odenberger, E.L., Hertzman, J., Thilderkvist, P., Merklein, M., Kuppert, A., Stöhr, T., Lechler, J., Oldenburg, M., 2012. Thermo-mechanical sheet metal forming of aero engine components in Ti–6Al–4V – Part 1: material characterisation. Int. J. Mater. Form., 1–12.
Olsen, R.H., Moreen, H.A., 1973. Calculation of the elastic anisotropy of Ti–6Al–4V alloy sheet from pole figure data. Metall. Trans. 4, 701–705.
Peirs, J., 2012. Experimental Characterisation and Modelling of the Dynamic Behaviour of the Titanium Alloy Ti6Al4V. PhD Thesis. Ghent University, Belgium.
Peirs, J., Verleysen, P., Degrieck, J., Coghe, F., 2010. The use of hat-shaped specimens to study the high strain rate shear behaviour of Ti–6Al 4V Int. J. Impact Eng. 37, 703–714.
Plunkett, B., Lebensohn, R.A., Cazacu, O., Barlat, F., 2006. Anisotropic yield function of hexagonal materials taking into account texture development and anisotropic hardening. Acta Mater. 54, 4159–4169.
Plunkett, B., Cazacu, O., Barlat, F., 2008. Orthotropic yield criteria for description of the anisotropy in tension and compression of sheet metals. Int. J. Plasticity 24, 847–866.
Porntadawit, J., Uthaisangsuk, V., Choungthong, P., 2014. Modeling of flow behavior of Ti–6Al–4V alloy at elevated temperatures. Mater. Sci. Eng. A 599, 212–222.
Rack, H.J., Qazi, J.I., 2006. Titanium alloys for biomedical applications. Mater. Sci. Eng. C 26, 1269–1277.
Simo, J.C., Hughes, T.J.R., 1986. On the variational foundations of assumed strain methods. J. Appl. Mech., ASME 53, 51–54.
Sukumar, G., Bhav Singh, B., Bhattacharjee, A., Siva Kumar, K., Gogia, A.K., 2013. Ballistic impact behaviour of β-CEZ Ti alloy against 7.62 mm armour piercing projectiles. Int. J. Impact Eng. 54, 149–160.
Tromans, D., 2011. Elastic anisotropy of HCP metal crystals and polycrystals. Int. J. Res. Rev. Appl. Sci. 6, 462–483.
Tuninetti, V., Habraken, A.M., 2014. Impact of anisotropy and viscosity to model the mechanical behavior of Ti–6Al–4V alloy. Mater. Sci. Eng. A 605, 39–50.
Tuninetti, V., Gilles, G., Péron-Lührs, V., Habraken, A.M., 2012a. Compression test for metal characterization using digital image correlation and inverse modeling. Procedia IUTAM 4, 206–214.
Tuninetti, V., Gilles, G., Milis, O., Lecarme, L., Habraken, A.M., 2012b. Compression test for plastic anisotropy characterization using optical full-field displacement measurement technique. In: Steel Res. Int. SE: 14th Int. Conf. Metal Forming 2012, pp. 1239–1242.
Vanderhasten, M., Rabet, L., Verlinden, B., 2008. Ti–6Al–4V: deformation map and modelisation of tensile behavior. Mater. Des. 29, 1090–1098.
Verma, R.K., Kuwabara, T., Chung, K., Haldar, A., 2011. Experimental evaluation and constitutive modeling of non-proportional deformation for asymmetric steels. Int. J. Plasticity 27, 82–101.
Yoon, J., Cazacu, O., Mishra, R.K., 2013. Constitutive modeling of AZ31 sheet alloy with application to axial crushing. Mater. Sci. Eng., A 565, 203–212.
Yoon, J.W., Lou, Y., Yoon, J., Glazoff, M.V., 2014. Asymmetric yield function based on the stress invariants for pressure sensitive metals. Int. J. Plasticity 56, 184–202.